Original Research Article

Numerical study of supercritical CO$_2$ and proppant transport in different geometrical fractures

Haizhu Wang, Meng Wang (iD)**, Bing Yang, Qun Lu, Yong Zheng and Heqian Zhao**, State Key Laboratory of Petroleum Resource and Prospecting, China University of Petroleum, 102249 Beijing, China

Abstract: Supercritical CO$_2$ (SC-CO$_2$) fracturing, as a kind of waterless fracturing method, is an effective treatment in the unconventional oil and gas industry. Due to its characteristic lower viscosity, supercritical CO$_2$ fracturing is likely to create thin and long fractures that connect pre-existing natural fractures and generate complex fractures. It is therefore very challenging to predict how far supercritical CO$_2$ carrying proppant can go and how proppant will be transported in natural fractures, when natural fractures are contacted or penetrated by induced fractures. In this paper, proppant transport with supercritical CO$_2$ in fractures was analyzed using the computational fluid dynamics method. Three types of fractures – planar fractures, T-shape fractures and crossing-shape fractures – were modeled. Five parametrical cases were studied using the T-shape and crossing-shape models. Results show that, for T-shape fracture cases, a turbulent flow regime might develop at a fracture junction, which can make proppant propagate to natural fractures. For crossing-shape fractures, a turbulent flow takes place behind the fracture junction, which causes a little sand dune to form downstream of the induced fracture. With the reduction in the width of the natural fracture, the height of the sand bank at the thinner natural fracture is higher than that at the wider natural fracture. Using a proppant whose density and diameter are respectively less than 1540 kg/m^3 and 0.25 mm, as well as a sand-carrying fluid whose sand ratio ranges from 8% to 10% and injection rate exceeds 2 kg/s, is beneficial to prop natural fractures. Moreover, the larger the intersection angle of the crossing-shape fracture is, the more difficult it is for proppant to enter natural fractures. This study reveals the influence of fracture geometry on proppant transport with SC-CO$_2$. © 2018 Society of Chemical Industry and John Wiley & Sons, Ltd.

Keywords: supercritical CO$_2$ fracturing; proppant transport; T-shape fracture; crossing-shape fracture; multiphase flow

Introduction

Large-scale hydraulic fracturing has led to the commercial development of unconventional reservoirs. Water is the primary component used for large-scale hydraulic fracturing, which gives rise to a series of issues such as reservoir damage, subsurface water pollution, and water scarcity.[1–3] To solve these problems, researchers began to explore the use of nonaqueous fracturing fluids (e.g., hydrocarbons and supercritical CO$_2$). Due to its unique characteristics, supercritical CO$_2$ is regarded as a promising working fluid in oil and gas extraction; for example, SC-CO$_2$ is able to generate numerous and complicated fracture

networks in formations, which can lead to a high conductivity path for production enhancement and flow-resistance reduction.[4–6]

Natural fractures occur widely in shale formations. As the results of SC-CO$_2$ fracturing experiments have indicated, SC-CO$_2$ tends to generate thinner and wavelike cracks with more secondary branches owing to its lower viscosity.[7–9] Consequently, it is inevitable that induced fractures will be contacted or penetrated by natural fractures. The interactions between induced fractures and natural fractures can make the extent of proppant transport difficult to predict.[10] As in the case of slick-water fracturing, one of the main concerns during the SC-CO$_2$ fracturing process is therefore proppant transport and placement in such fractures. Several studies on proppant transport in complex fracture networks were conducted recently. Sahai *et al.* fabricated lab-scale experimental apparatus to evaluate proppant flow in secondary fractures and concluded that proppant was able to flow in secondary fractures by drag force of the fluid or rolling into them as a result of the effect of gravity.[11] Alotaibi *et al.* extended this work and highlighted the mechanism of proppant transport during proppant bed development; they further included friction loss and proposed a scalable correlation for 30/70 brown sands to estimate the equilibrium sand bed height for different flow rates and sand concentrations.[12] Tong and Mohanty studied the proppant transport in fractures with different types of bypass angle, considering the effects of shear rate and proppant size. They revealed that proppant in secondary fractures increases with the increase in the shear rate and the reduction in the bypass angle.[13] Wen *et al.* used a self-designed complex fracture simulation device to study proppant migration and the settling law in a complicated fracture network.[10] They pointed out that the fracturing fluid's carryover effect plays a major role in the process of sandbank formation in secondary fractures near the wellbore, while the gravity effect dominates in secondary fractures far away from the wellbore.

Compared to other fracturing fluids, SC-CO$_2$ has relatively lower viscosity, so its proppant-carrying ability is not clear.[14] So far, very limited research exists in the literature about the two-phase flow of SC-CO$_2$ and proppant. To study the performance of SC-CO$_2$ carrying proppant, Hou *et al.* used experimental method and theoretical analysis to derive the terminal velocity of particle settling in SC-CO$_2$ fluid whose Reynold number ranges from 1000 to 5000. And the

model can predict the characteristics of proppant sedimentation in the fractures.[15] Guo conducted a numerical simulation of proppant transport with SC-CO$_2$ in horizontal coiled-tubing and facturing fracture to validate the feasibility of SC-CO$_2$ carrying proppant.[16] Furthermore, to evaluate the horizontal sand-carrying performances of SC-CO$_2$, Hou *et al.* introduced the concept of following performance and established an calculation model that is based on the classic BBO(Basset-Boussinesq-Ossen) equation to analyze the following performance of proppant in SC-CO$_2$ fluid. Experimental results were also used to verify the correctness of the calculation.[17] Hou *et al.* proposed the cotangent of particle landing angle which was used to evaluate the thicken performance of SC-CO$_2$. The particle-settling velocity was found to determine the particle-transporting distance and also the transporting capability of SC-CO$_2$.[18]

Previous research concentrated on the feasibility of proppant transport with SC-CO$_2$ in fracturing fractures. However, previous numerical models were usually limited to planar fracture cases and pre-existing natural fractures were not taken into consideration. Moreover, the effects of complex fracture geometry and the width of secondary slots on the proppant transport and deposition of SC-CO$_2$ fracturing in the cross fractures are not well understood. In a paper based on the Eulerian-granular model (EGM), a CFD (Computation Fluid Dynamic) model was established to simulate proppant transport with SC-CO$_2$ in different fracture geometric profiles, and the interactions between proppant particles and SC-CO$_2$ fluid were coupled in the models.[19] Three types of fracture geometry – a planar fracture, a fracture with a T-junction, and a crossing junction – were simulated. Sensitivity analysis was also performed to investigate how proppant transport is affected by injection rate, proppant density, sand ratio, mass flow rate and crossing angle. In this way the research was able to provide a basis for parametric optimization and technological adaptation of SC-CO$_2$ fracturing.

Modeling

Proppant transport in SC-CO$_2$ fracturing fluid involves complex fluid dynamics and multiphase interactions, coupled with a complex fracture system. Many modeling and simulation studies have been reported recently that studied slick water fracturing. This indicates that the CFD method can be used for

studying the interactions between SC-CO₂ and proppant.[20–22] Moreover, there are two ways to simulate multiphase flow in CFD simulation.

One is the Eulerian-granular model (EGM), which is a Eulerian-Eulerian approach that treats the particle phase as a concentration field and incorporates the kinetic theory of granular flow (KTGF) for particle flow. The KTGF is one of the most significant theories for simulating particle flow. Granular temperature, which accounts for the random motion of particles, is the key concept in this theory. Energy dissipates during random collisions between particles.[23,24]

The other is the Lagrangian model, which treats the second phase as a discrete collection of individual particles. As the Lagrangian model is required to solve multiple independent trajectories, the computation cost is higher than the Eulerian approach.

This study adopted the EGM, which can describe the flow behavior of SC-CO₂ and proppant and reduce computation costs. In the EGM, a single pressure is shared by all phases. A separate system of mass momentum and energy equations is solved for each of the phases. Coupling of phases occurs through pressure and the so-called interphase mass, momentum, and energy-exchange coefficients. In addition, due to the sensitivity of SC-CO₂ to temperature and pressure, the Aungier–Redlich–Kwong model was adopted to solve the density of SC-CO₂.[25]

Governing equations

In the EGM, the continuity, momentum and energy equations are given as Eqns (1) to 3.[19] The continuity equation is given by Eqn (1)

$$\frac{\partial}{\partial t}(\alpha_q \rho_q) + \nabla \cdot (\alpha_q \rho_q \vec{v}_q) = 0 \quad \sum_1^N \alpha_q = 1.0 \quad (1)$$

where, α_q is the volume fraction of component q, $\vec{v}_q$ is the velocity vector for the phase q (l: liquid phase, s: solid phase), ρ_q is the density.

The momentum equation for a phase l fluid is given by Eqn (2):

$$\frac{\partial}{\partial t}(\alpha_l \rho_l \vec{v}_l) + \nabla \cdot (\alpha_l \rho_l \vec{v}_l \vec{v}_l)$$

$$= -\alpha_l \nabla p + \nabla \cdot \overline{\overline{\tau}}_l + \alpha_l \rho_l \vec{g} + K_{sl}(\vec{v}_s - \vec{v}_l) \quad (2)$$

The momentum equation for a solid phase s is given by Eqn (3):

$$\frac{\partial}{\partial t}(\alpha_s \rho_s \vec{v}_s) + \nabla \cdot (\alpha_s \rho_s \vec{v}_s \vec{v}_s)$$

$$= -\alpha_s \nabla p + \nabla \cdot \overline{\overline{\tau}}_s + \alpha_s \rho_s \vec{g} + K_{ls}(\vec{v}_s - \vec{v}_l) \quad (3)$$

in which,

$$\overline{\overline{\tau}}_q = \alpha_q \mu_q (\nabla \cdot \vec{v}_q + \nabla \cdot \vec{v}_q^T) + \alpha_q \left(\lambda_q - \frac{2}{3}\mu_q\right) \nabla \cdot \vec{v}_q \overline{\overline{I}}$$

where $\vec{g}$ is the acceleration vector; q is the phase label, which represents liquid phase l or solid phase s, μ_q and λ_q are shear and bulk viscosity; $\vec{v}_q$ is a flow velocity vector for liquid and solid phases; P is the pressure shared by both liquid and solid phases; and K_{sl} is the phase momentum exchange coefficient between liquid phase l and solid phase s.

The energy equation is given by Eqn (4):

$$\frac{\partial}{\partial t}\left(\sum_{p=1}^2 \alpha_q \rho_q E_q\right) + \nabla \cdot \sum_{k=1}^2 (\alpha_q \vec{v}_q(\rho_q E_q + P)$$

$$= \nabla \cdot (k_{eff} \nabla T) \quad (4)$$

where, E_p is the energy of phase q; k_{eff} is the effective conductivity; and T is the temperature, K.

There are many empirical drag laws to describe the fluid viscous force on solid particles in CFD software – for example Gidaspow, Wen Yun, and Syamlal–O'Brien. Kong adopted the Gidaspow model to simulate proppant transport in fractures and eventually gained insight into the complexity of slurry flow.[21] According to the theory guide, the model has the same form for a diluted system with liquid volume fraction α_l and the following expression is proposed for a dense particle system with $\alpha_l < 0.8$, the phase momentum exchange coefficient:

$$K_{sl} = \frac{150\alpha_l(1-\alpha_l)\mu_l}{\alpha_l d_s^2} + \frac{1.75\alpha_l \alpha_s}{d_s}\left|\vec{v}_s - \vec{v}_l\right| \quad (5)$$

The solid phase viscosity is calculated based on the KTGF using granular temperature. In the KTGF, the solid shear viscosity (μ_s) includes kinetic $\mu_{s,kin}$, collisional $\mu_{s,col}$, and frictional components $\mu_{s,fri}$, and the three terms correspond to dilute, intermediate, and dense systems, respectively. Due to the viscosity limitation of SC-CO₂, the sand-carrying fluid used for SC-CO₂ fracturing is usually a dilute system. The solid shear viscosity therefore only depends on the former
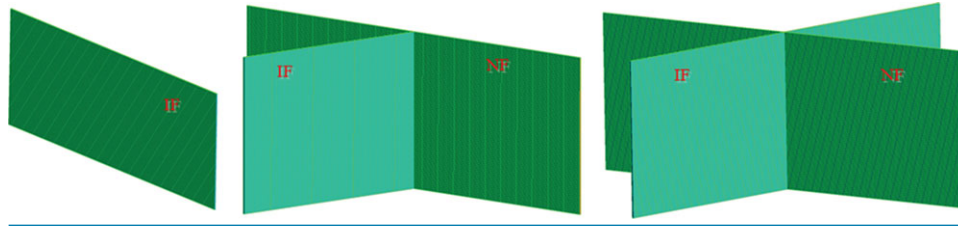
Figure 1. Modeled fracture geometries (from left: planar, fracture with a T-junction, and fracture with a crossing junction; IF – induced fracture; NF – natural fracture).

two parts. Bulk viscosity λ_s and radial distribution function (g_0) are calculated with the approach used by Lun. According to the kinetic theory of dense gas, solid pressure (p_s) includes kinetic and collisional terms. The closure equations are listed in Eqn (6)–(11):[20]

$$\mu_s = \mu_{s,kin} + \mu_{s,col} \tag{6}$$

$$\mu_{s,kin} = \frac{10 d_s \rho_s \sqrt{\Theta_s \pi}}{96 \alpha_s g_0 (1+e)} \left[1 + \frac{4}{5} \alpha_s g_0 (1+e) \right]^2 \tag{7}$$

$$\mu_{s,col} = \frac{4}{5} \alpha_s d_s \rho_s g_0 (1+e) \left(\frac{\Theta_s}{\pi} \right)^{\frac{1}{2}} \tag{8}$$

$$\lambda_s = \frac{4}{3} \alpha_s d_s \rho_s g_0 (1+e) \left(\frac{\Theta_s}{\pi} \right)^{\frac{1}{2}} \tag{9}$$

$$g_0 = \left(1 - \left(\frac{\alpha_s}{\alpha_{s,max}} \right)^{\frac{1}{3}} \right)^{-1} \tag{10}$$

$$p_s = \alpha_s \rho_s \Theta_s + 2\alpha_s^2 \rho_s \Theta_s g_0 (1+e) \tag{11}$$

The solid pressure term, shear viscous term, and bulk term are computed from the KTGF based on the conservation of the kinetic energy of moving particles. The equation, which is solved in its algebraic form by ignoring the convection and diffusion terms in the CFD software in order to avoid instability, is given by:

$$\frac{3}{2} \left[\frac{\partial}{\partial t} (\alpha_s \rho_s \Theta_s) + \nabla \cdot (\alpha_s \rho_s v_s \Theta_s) \right]$$
$$= \left(-p_s \overline{\overline{I}} + \overline{\overline{\tau}}_s \right) : \nabla \overrightarrow{v_s} - \nabla \cdot (k_\Theta \nabla \Theta_s) - \gamma + \Phi \tag{12}$$

Here, Θ_s is granular temperature; k_Θ is granular energy diffusion. The coefficient γ is the collisional dissipation of energy; Φ is interphase energy exchange.

Geometrical models

Many laboratory SC-CO₂ fracturing experiment results found that the fracture induced by SC-CO₂ had more branches along the main fracture, indicating that induced fracturing with a lower viscosity fluid forms a more complex fracture network in rocks.[26,27] Due to the fact that our research only focuses on SC-CO₂ and proppant transport, we simplified the fracture network to typical elements and modeled fractures as parallel planes, which has been done by many previous researchers. Based on the fracture parameters in the literature, we used simulation fractures for different geometries, which are shown in Fig. 1; their geometric parameters are listed in Table 1.[28,29] Meshing mode of model adopted the structured grid partition method, which can enhance the precision of calculations and the rate of convergence. For the planar fracture case, sand-carrying fluids entered the calculation domain from the left side of the induced fracture and exited from the right side; for the multiple-fracture case, fracturing fluids flow into calculation area only through the left side of the induced fracture.

Initial and boundary conditions

A mass flow inlet was used as an inlet boundary condition, and different mass flow rates were imposed on the calculation domain. A pressure outlet was used as an outlet boundary condition. A no-slip wall boundary was set for all phases. Considering the lower permeability of unconventional reservoirs, the filtration loss of SC-CO₂ was ignored. The outlet pressure boundary conditions were set to 20 MPa. To improve calculation precision, turbulence intensity and hydraulic diameter at both inlets and outlets were set correspondingly. The phase-coupled SIMPLE algorithm was applied for pressure–velocity coupling, the gradient was discretized with the least-squares cell-based method, pressure used a standard scheme

Table 1. Model geometry inputs.

		T junction		Crossing junction	
	Planar	IF	NF	IF	NF
Length (mm)	3000	1500	3000	3000	3000
Height (mm)	1000	1000	1000	1000	1000
Width(mm)	10	10	10	10/6	10

Notes: IF – induced fracture; NF – natural fracture.

Table 2. Parametric matrix of numerical simulation.

	Proppant density (kg/m³)	Sand ratio (%)	Proppant diameter (mm)	Mass flow rate (kg/s)	Crossing angle
Proppant density (kg/m³)	1540/1750/2040/2350	8	0.25	2	1540
Sand ratio	1540	2/4/8/10	0.25	2	0.08
Proppant diameter (mm)	1540	8	0.25/0.3/0.425/0.5	2	0.25
Mass flow rate (kg/s)	1540	8	0.25	1.5/2/3/4	2
Crossing fracture angle	1540	8	0.25	2	45°/60°/90°

for discretization, and other variables were treated with the first order upwind scheme.

The parameter matrix of numerical simulation indicated in Table 2 was determined according to previous research on proppant transport with fracturing fluid of low viscosity.[30–32] The benchmark simulation condition has a proppant density of 1540 kg/m³, proppant diameter of 0.25 mm, sand ratio of 0.08, and mass flow rate of 2 kg/s. The numerical simulation was divided into four groups in general. For each group of numerical simulation, the proppant distribution characteristic was analyzed. This is located in the central plane on the fracture width direction.

Results and discussions

Laws of proppant transport with SC-CO₂ in different geometric fractures

T-shape case

Figure 2 illustrates the proppant distribution within the induced fracture and natural fracture of T-shape fracture under the benchmark condition. From the proppant distribution contour within the natural fracture of the T-shape fracture case, proppant that has reached the T-junction is successfully carried into the natural fracture and evenly distributed to each wing on both sides of it. This is because the same boundaries were set for the two natural fracture wings. It can be

seen that the profile of suspension zone formed by proppant transport with SC-CO₂ appears as a symmetrical ridge. The possible reason for this is that, within the induced fracture, the proppant velocity along the natural fracture plane direction is zero before it reaches the junction. After proppant grains enter the natural fracture plane, they start an acceleration process along the natural plane due to a velocity gap with SC-CO₂, and proppant velocity keeps increasing to a force equilibrium state. With the increase in injection time, the profile of the suspension zone is steeper near the junction and then it becomes shallow.

Crossing-shape case

Figure 3 illustrates the proppant distribution within the induced fracture and natural fracture of a crossing fracture under the benchmark conditions. When proppant transport with SC-CO₂ reaches the crossing junction, the sand-laden fluid is divided into three streams: the downstream of induced fracture and on both sides of the natural fracture. At the initial stage of the injection of the particles into the crossing fracture ($t = 10$ s), many particles accumulated in the induced fracture close to the intersections, then a small quantity of the accumulated particles were dragged into the natural fracture, while most of them continued to move forward along the induced fracture. Next, with an increase in injection time, more and more proppant
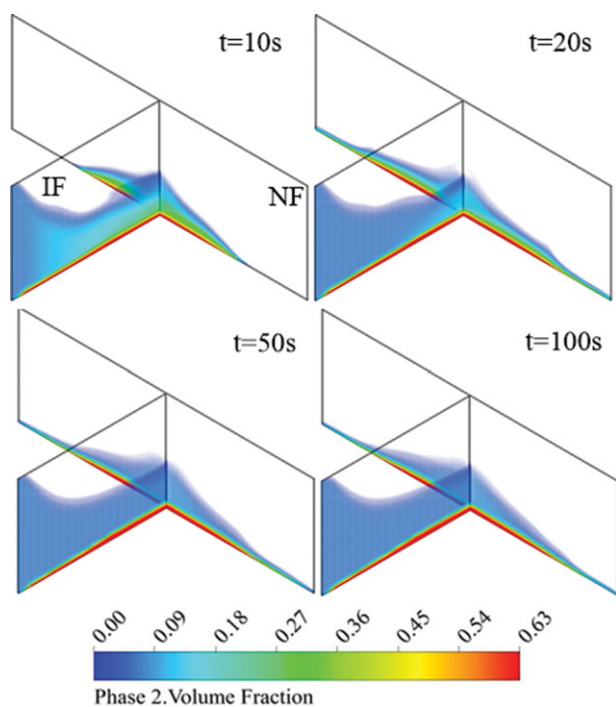
Figure 2. Volume rendering of the volume fraction of particles at 10 s, 20 s, 50 s, and 100 s for the T-shape fracture case (IF – induced fracture; NF – natural fracture).
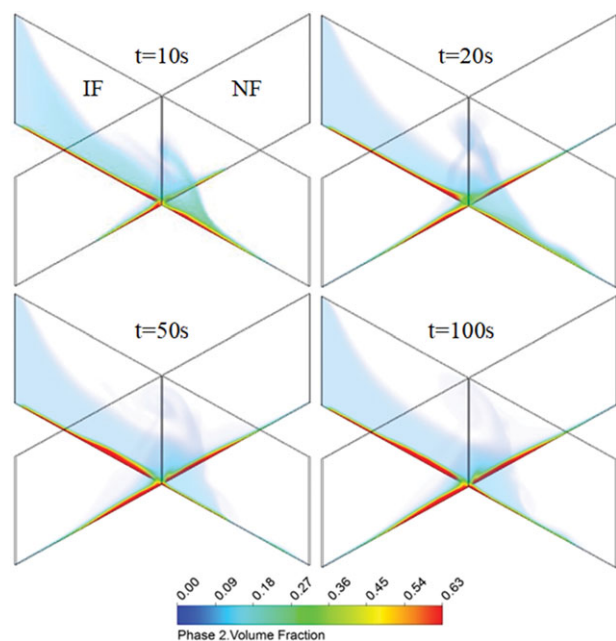

Figure 3. Volume rendering of the volume fraction of particles at 10 s, 20 s, 50 s, and 100 s for the crossing-shape fracture case (IF – induced fracture; NF – natural fracture).

was transported, accumulating progressively along the natural fracture, evenly distributed on each wing on both sides of the natural fracture. The height of the sand bank that is formed ahead of the junction within the induced fracture was thicker than that downstream of the induced fracture. The reason is that, with an increase in injection time, the intensity of the turbulent flow downstream of the induced fracture is strengthened gradually, leading to the reduction in the particle's settlement and deposition.

As we know in real field cases, the width of a natural fracture is usually smaller than that of an induced fracture. To investigate the effects of the width of a natural fracture on particles' deposition in a crossing-shape fracture, the width of induced fracture is therefore kept constant. The bypass angle between the induced fracture and the natural fracture is 90° and the width of the induced fracture and natural fracture are 10 mm and 6 mm, respectively. Figure 4 shows the particle volume fraction in the crossing-shape fracture from 10 s to 100 s, when the width of the natural fracture is 10 mm and 6 mm respectively. With the reduction in the width of the natural fracture, the movement length of the particles decreased and more particles settled and accumulated at the induced fracture. Meanwhile, the height of the sand bank at the thinner natural fracture is higher than that at the wider natural fracture. This is because, with the decrease in the width of the natural fracture, the interactions between the proppants and the fracture face strengthen gradually, leading to the settlement of more particles. For the crossing-shape fracture, the thinner the natural fracture is, the worse is the placement efficiency of the proppant.

Comparison of proppant distribution in different types of fracture models

Figure 5 illustrates the proppant distribution in the induced and natural planar, T-shape and crossing fractures in the benchmark condition. In the planar fracture case, with the continuous injection of SC-CO₂ and proppant, part of the sand has settled at the bottom of the fracture and formed a sand dune due to the effect of sand gravity. Comparing the proppant distribution within the induced fracture to the equivalent part of the planar case suggests that the sand area formed before the junction is slightly thinner, indicating that more proppant is likely to have moved into the natural fracture. One possible explanation for the
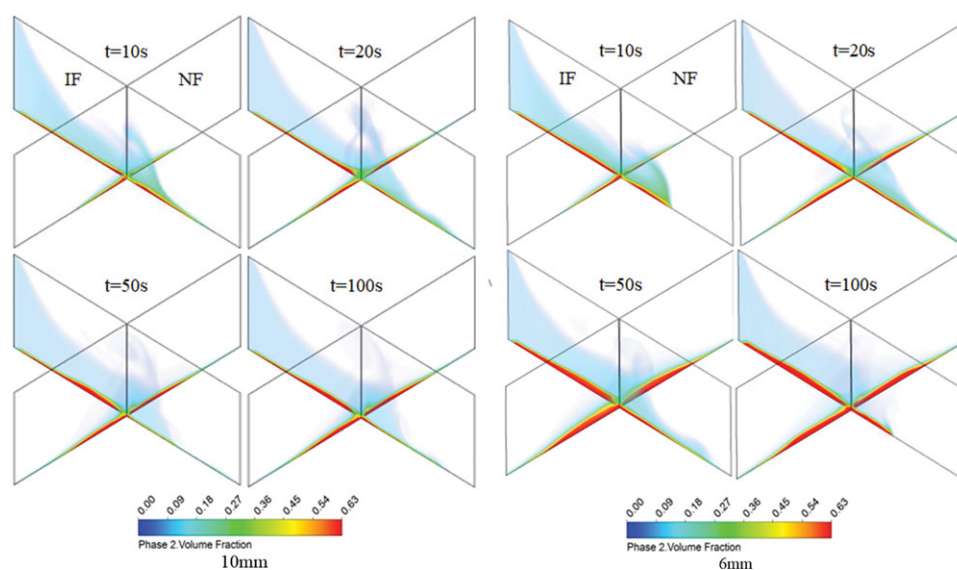
Figure 4. Volume rendering of the volume fraction of particles at 10 s, 20 s, 50 s, and 100 s in the crossing-shape fracture with different widths (10 mm, 6 mm) of natural fracture (IF – induced fracture; NF – natural fracture).
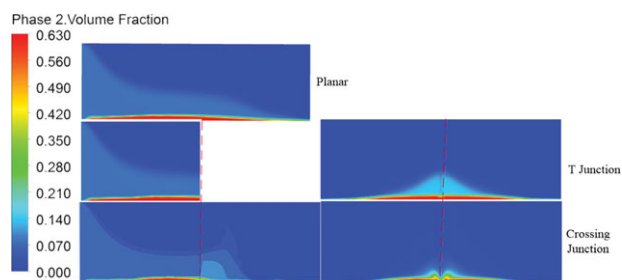

Figure 5. The proppant distribution contours of different fracture models after 100 s injection (left side – induced fracture; right side – natural fracture; red dashing – crossing junction).

phenomenon is that a turbulent flow regime might develop in the junction, which is detrimental to dune forming but helpful for carrying proppant particles into a natural fracture.

Comparing the crossing facture case with the previous two cases, a sand dune that has formed ahead of the junction in induced fracture is thicker, while the height of immobile sand bed appears much thinner and the suspension layer has a relatively wide range downstream of the induced fracture. This is because, before the proppant transport with SC-CO$_2$ reaches the junction, the horizontal velocity of proppant declines owing to the impact of the perpendicular intersection with the natural fracture; proppant therefore deposits at the bottom of the fracture and forms a relatively

thick sand dune, which causes the velocity of sand-laden fluid to increase. A turbulent flow regime might develop after sand-carrying fluid flows downstream of the induced fracture where proppant particles are suspended and do not form sand dunes.

It might also be noted that there are some differences in proppant distribution among the natural, T-shape, and crossing-shape fracture cases, but proppant is evenly and symmetrically distributed between the two wings of a natural fracture. Due to the fact that the velocity of sand-carrying fluid at the junction is greater, the height of sand dunes at the crossing-shape fracture position is reduced. After proppant grains enter the natural fracture plane, the velocity of proppant decreases near the junction, leading to relatively higher sand dunes.

Analysis and discussion

To obtain rules for the placement and filling of proppant in different complex fractures, the relationship between the dimensionless height of the sand area and the dimensionless fracture length of natural fractures in T-shape and crossing-shape fractures were analyzed in this paper. Parameters were analyzed and optimized according to their impact on the capability of proppant transport with SC-CO$_2$. We found that the proppant distribution in natural fractures was symmetrical. The following data analysis was therefore taken from a wing of a natural fracture.
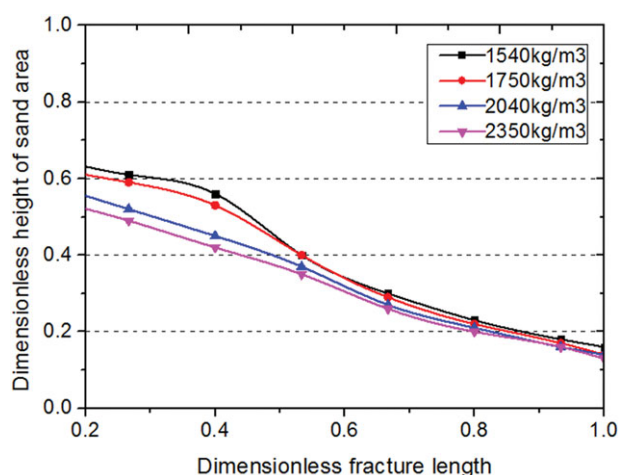
Figure 6. The relationship curve between the dimensionless sand area height and the dimensionless fracture length for the T-shape fracture case.
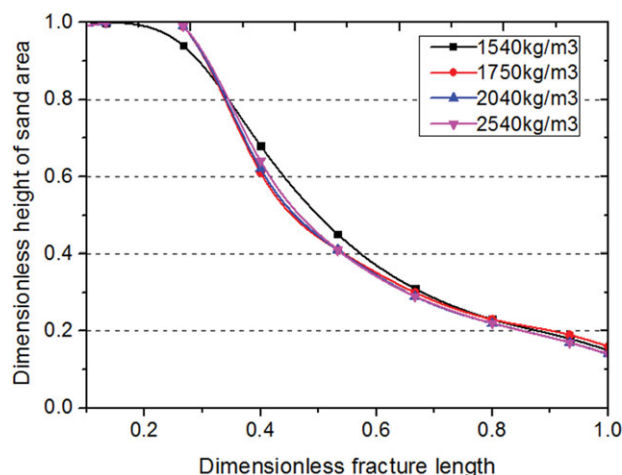

Figure 7. The relationship curve between the dimensionless sand area height and the dimensionless fracture length for the crossing-shape fracture case.

The dimensionless fracture length refers to the ratio of the distance away from the fracture junction to the half fracture length, while the dimensionless height of the sand area reflects the filling effect of proppant in fractures.

Proppant density

Figure 6 shows the relationship between the dimensionless height of the sand area and the dimensionless fracture length under a different proppant density for a T shape. As indicated in Fig. 6, as the migration distance of SC-CO₂ carrying proppant in the natural fracture increases, the dimensionless height of the sand area in the fracture gradually decreases, approaching a linear relationship. This is because, as the sand-laden fluid continues to move further, the horizontal velocity declines correspondingly. Moreover, when the dimensionless fracture length ranges from 0 to 0.5, the dimensionless height of the sand zone decreases with an increase in proppant density, which means that the larger the proppant density, the more difficult it is for proppant to enter the natural fracture, thus effectively supporting it. When the dimensionless fracture length is greater than 0.5, the proppant density exerts no great impact on the range of the sand-bearing area in fracture. This is because, as SC-CO₂ carries the proppant into a certain depth of the fracture, the proppant density is no longer the primary factor to cause the differences in settlement and distribution in the fracture due to the limitation of the flow rate. During SC-CO₂ fracturing treatment, the

lightweight proppant is therefore recommended as it could be beneficial to prop natural fractures.

Figure 7 shows the relationship between the dimensionless height of the sand area and the dimensionless fracture length under different proppant densities for the crossing shape. For the crossing-shape fracture case, the dimensionless height of sand area within the natural fracture gradually decreases with the increase in the migration distance of the SC-CO₂ carrying proppant. This is because, as the sand-laden fluid continues to move to a deeper location, its horizontal velocity declines continuously. Moreover, no matter how heavy or light the proppant is, the proppant density has no obvious influence on the range of sand area in the natural fractures in the crossing-shape fracture case.

Proppant size

As indicated in Fig. 8, in the T-shape fracture case, as the migration distance of SC-CO₂ carrying proppant along the natural fracture increases, the dimensionless height of the sand area gradually decreases, approaching a linear relationship. The descending slope of the curve varies according to the proppant size. When the dimensionless fracture length is fixed at a certain value, we also find that the dimensionless height of the sand zone decreases gradually with an increase in the proppant particle size. That means that the larger the proppant size is, the more difficult it is for proppant to enter the natural fracture. Meanwhile, the descending slope of curve decreases with the increase
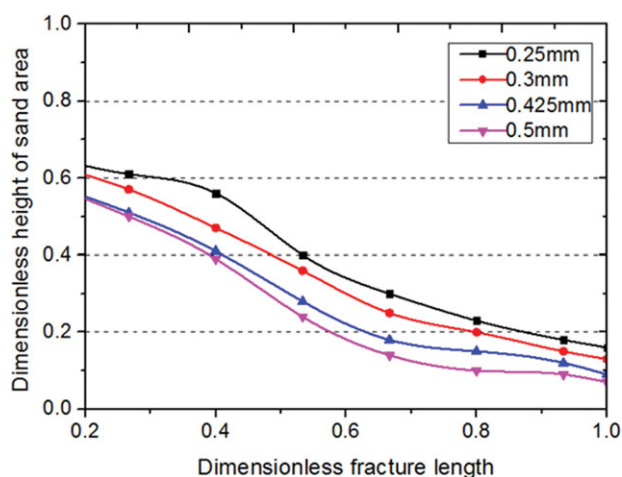
Figure 8. The relationship curve between the dimensionless sand area height and the dimensionless fracture length for the T-shape fracture case.
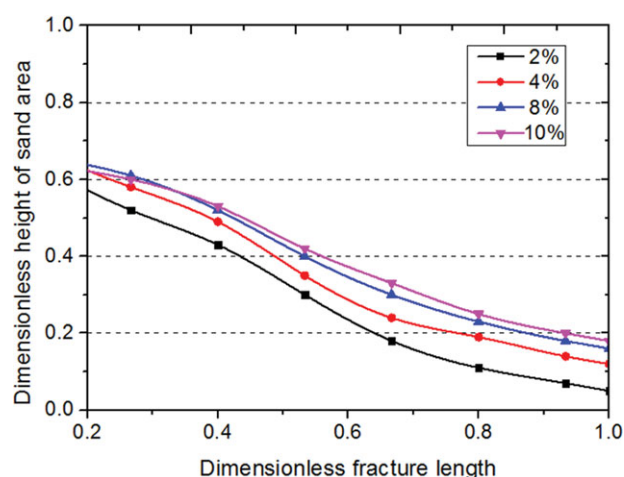

Figure 10. The relationship curve between the dimensionless sand area height and the dimensionless fracture length for the T-shape fracture case.
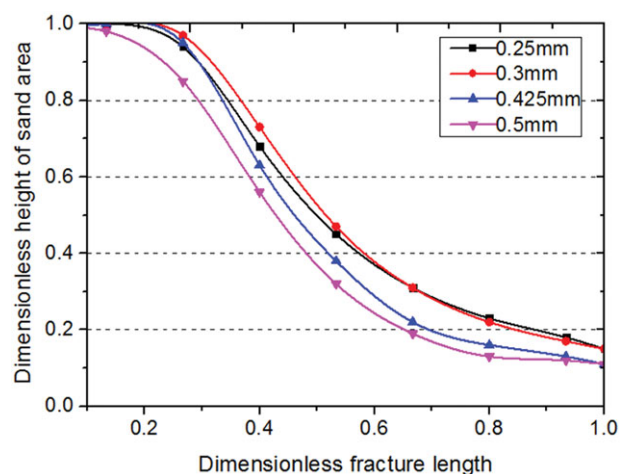

Figure 9. The relationship curve between the dimensionless sand area height and the dimensionless fracture length for the crossing-shape fracture case.

in the proppant's particle size, because the larger the proppant size, the easier it is for the proppant to be affected by the surface of the fracture wall, leading to a steeper profile of the sand zone. In the case of the T-shape fracture, therefore, the smaller proppant grain size is better for sand placement.

Figure 9 shows that the relationship between the dimensionless height of the sand area and the dimensionless fracture length with the variation of proppant size. In Fig. 9, for the crossing-shape fracture case, with an increase in the transport distance of sand-carrying fluid within the natural fracture, the sand area gradually decreases. This is because, as the sand-laden fluid continues to move deeper, the

horizontal velocity of the proppant declines. For the larger size particle (0.425 mm–0.45 mm), the dimensionless height of the sand area decreases at the location of the natural fracture, and the proppant size increases. On the other hand, for the smaller sand particles (0.25 mm–0.3 mm), such a law does not obviously apply. Even so, the dimensionless height of sand area formed by the smaller sand particles is higher than that formed by the larger particles. This fact reveals that the smaller sand particles are useful to enhance sand placement in the crossing-shape fracture case.

Sand ratio

As shown in Fig. 10, for the T-shape fracture, as the distance of proppant transport with SC-CO₂ in the natural fracture increases, the sand-filling area decreases gradually. With different sand ratios, the slopes of sand area are all approximately similar. As the proppant transport with SC-CO₂ arrives at the same location, the dimensionless height of the sand zone increases gradually, with the increasing sand ratio. This is because, as the sand ratio increases, the interactions between proppant particles and the surface of the fracture wall are intensified, leading the proppant to deposit more easily. Moreover, the gap of varied curves under different sand ratios is gradually narrowing with the increase of sand ratio. Apparently, as the sand ratio of sand-laden fluid ranges from 8% to 10%, the distribution rule of proppant transport with SC-CO₂ begins to vary gently within natural fracture in T-shape
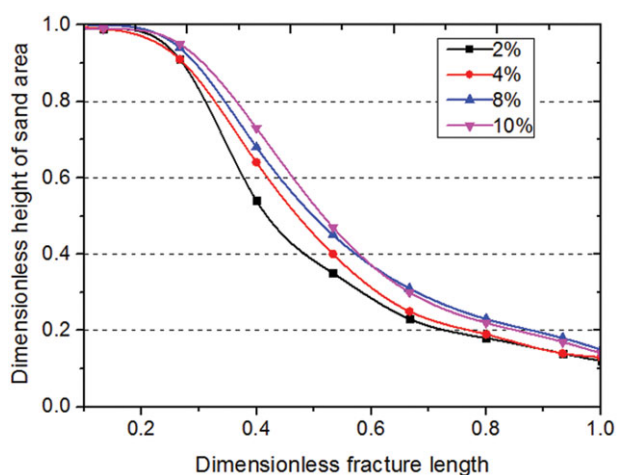
Figure 11. The relationship curve between the dimensionless sand area height and the dimensionless fracture length for the crossing-shape fracture case.
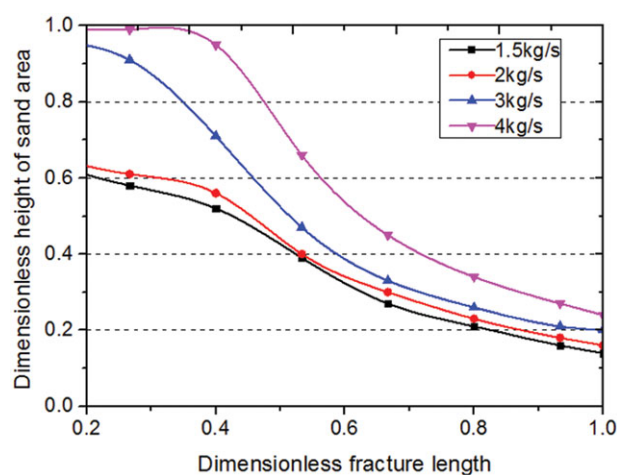

Figure 12. The relationship curve between the dimensionless sand area height and the dimensionless fracture length for the T-shape fracture case.

Figure 13. The relationship curve between the dimensionless sand area height and the dimensionless fracture length for the crossing-shape fracture case.

fracture, so it is advantageous for natural fracture to use sand-laden fluid with a sand ratio of 8% to 10%.

As shown in Fig. 11, for the crossing-shape fracture case, when the proppant transport with SC-CO₂ extends towards a deeper natural fracture, the sand area gradually decreases. As the interactions between the proppant grains and the inner wall of the fracture are intensified, the dimensionless height of the sand zone in the same location of the fracture increases gradually with an increase in the sand ratio. In addition, for lower sand ratios of sand-carrying fluid (2%-4%), if the dimensionless fracture length is fixed, there is a big difference in the dimensionless height of the sand area, whereas for larger sand ratios of sand-laden fluid (8%–10%), such a difference becomes much smaller than before. Consequently, for all sand ratio cases shown in Fig. 11, as a trend, the larger sand ratio (8%–10%) of SC-CO₂ fracturing fluid is a better choice for the crossing-shape fracture.

Mass flow rate

Figure 12 shows the relationship between the dimensionless height of the sand area and the dimensionless fracture length under different mass flow rates. For T-shape fractures, the dimensionless height of the sand area gradually decreases, as the proppant transport with SC-CO₂ moves into deeper locations. The total dimensionless height of the sand area formed by the larger mass flow rate is higher than that formed by the smaller rate, and the larger the mass

flow rate is, the steeper is the shape of the sand area within the natural fracture. This fact shows that the mass flow rate has a large impact on sand placement in the T-shape fracture case, and the increase in the mass of the proppant grain in per unit of time, due to the enhancement of the mass flow rate, can improve the fracture's supporting effect in natural fractures.

As shown in Fig. 13, for crossing shape fracture, the dimensionless height of sand area gradually decreases with proppant propagating along the natural fracture. However unlike the fracture with a T-junction, when the mass flow rate of sand-carrying fluid is larger (3 kg/s–4 kg/s), with an increase in the migration distance of proppant transport with SC-CO₂, the dimensionless
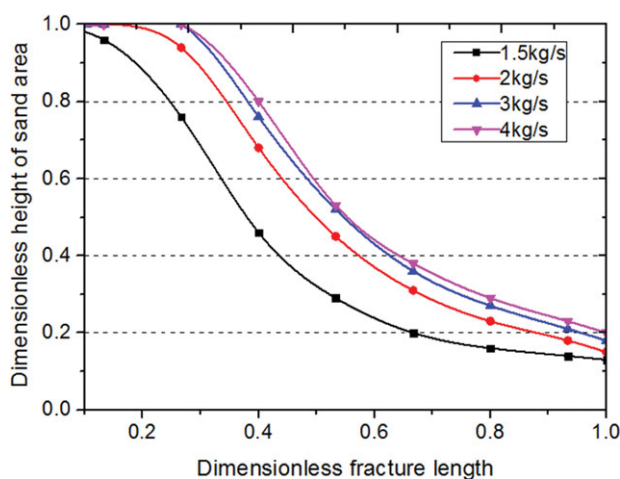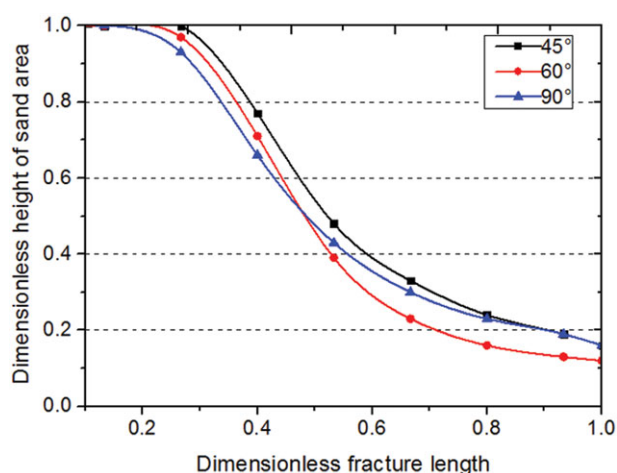
Figure 14. The relationship curve between the dimensionless sand area height and the dimensionless fracture length for the crossing-shape fracture case.

height of the sand area decreases slightly. On the other hand, when the mass flow rate is lower, the dimensionless height of the sand area decreases significantly, which is attributed to the shunting of the downstream part of induced fracture. Moreover, in the same location in the natural fracture, the dimensionless height of the sand area increases slightly with the increase of mass flow rate. This is because, when the mass flow rate reaches a certain value, the increase of downstream shunting of induced fracture has an adverse effect on the transporting capability of proppant in natural fracture. A mass flow rate of sand-laden fluid that is higher than 2 kg/s benefits sand placement to prop natural fracture during SC-CO$_2$ treatment.

Crossing angle

Figure 14 indicates the relationship between the dimensionless height of the sand zone, the dimensionless fracture length and the variation of crossing angle. It shows that with the migration distance of the proppant transport with SC-CO$_2$ increasing in the natural fracture, the sand area gradually decreases, and the descending slope of above varied curves under different intersection angles is similar. In addition, when we fix the value of dimensionless fracture length, with an increase in the intersection angle, the dimensionless height of the sand zone decreases gradually, which means that the larger the intersection angle is, the more difficult it is for the

proppant to enter a natural fracture in the crossing-shape fracture case.

Conclusion

In this research a CFD model was established based on the EGM to simulate proppant transport with SC-CO$_2$ in different geometrical fractures. To investigate how different parameters impact the proppant transport behavior with SC-CO$_2$ in complex fracture scenarios, five parametric cases, including proppant density, proppant size, sand ratio, mass flow rate and crossing angle, were studied using T-shape and crossing-shape models.

1. For a crossing-shape fracture, with a decrease in the width of the natural fracture, the movement length of the particles decreased and more particles settled and accumulated in the induced fracture. The height of the sand bank in a thinner natural fracture is higher than at a wider natural fracture.
2. Comparing to proppant distribution of planar fracture case, some proppant that has reached the junction of T shape fracture can be carried into intersected natural fracture. One possible reason is that turbulent regime might develop at the junction. For a crossing-shape fracture, a large portion of the proppant still remained in the induced fracture before the fracture junction, and a small part of proppant was carried into the natural fracture and was evenly distributed on both sides of the natural fracture. However, after the proppant reached the downstream part the of induced fracture, located behind the junction, proppant was suspended and almost no sand dune formed due to the turbulent flow.
3. Under the simulated conditions used in this study, it was beneficial, for propping a natural fracture, to use a proppant whose density and size were less than 1540 kg/m3 and 0.25 mm, respectively, as well as sand-carrying fluid whose sand ratio ranged from 8% to 10% and whose injection rate exceeded 2 kg/s.
4. Crossing-angle case studies suggest that the descending slopes of varied curves under different crossing angles show similar trend. Additionally, when proppant is transported toward the same location, with an increasing intersection angle, the dimensionless height of the sand zone decreases gradually, which means that the larger the intersection angle, the more difficult it is for

proppant to enter a natural fracture in the case of a crossing-shape fracture.

Acknowledgements

References

1. Middleton R, Carey J, Currier R, Hyman J, Kang Q, Karra S, *et al.*, Shale gas and non-aqueous fracturing fluids: opportunities and challenges for supercritical CO_2. *Appl Energy* **147**(3):500–509 (2015).

2. Rudyk S, Spirov P, Al-Hajri R and Vakili-Nezhaad G, Supercritical carbon dioxide extraction of oil sand enhanced by water and alcohols as Co-solvents. *J. CO_2 Util* **17**(1):90–98 (2017).

3. Liu S, Wang J, He H and Wang H, Mechanism on imbibition of fracturing fluid in nanopore. *Nanosci Nanotechnol Lett* **10**(21): 87–93 (2018).

4. Li X and Elsworth D, Geomechanics of CO_2 enhanced shale gas recovery. *J Nat Gas Sci Eng* **26**:1607–1619 (2015).

5. Ribeiro L, Li H and Bryant J, Use of a CO_2-Hybrid fracturing design to enhance production from unpropped-fracture networks. *SPE Hydraulic Fracturing Technology Conference (SPE-173380)*, The Woodlands, Texas, USA, February 3–5 (2015).

6. Sinal M and Lancaster G, Liquid CO_2 fracturing: advantages and limitations. *J Can Pet Technol* **26**(5):26–30 (1987).

7. Tudor R and Poleschuk A, Low-viscosity, low-temperature fracture fluids. *J Can Pet Technol* **35**(7):31–36 (1996).

8. Ishida T, Niwa T, Aoyagi K, Yamakawa A, Chen Y, Fukahori D, *et al.*, AE Monitoring of hydraulic fracturing laboratory experiment with supercritical and liquid state CO_2. *ISRM International Symposium (EUROCK 2012)*. Stockholm, Sweden, May 28–30 (2012).

9. Chen Y, Nagaya Y and Ishida T, Observations of fractures induced by hydraulic fracturing in anisotropic granite. *Rock Mech Rock Eng* **48**(4):1455–1461 (2015).

10. Wen Q, Wang S, Duan X, Li Y, Wang F and Jin X, Experimental investigation of proppant settling in complex hydraulic-natural fracture system in shale reservoirs. *J Nat Gas Sci Eng* **33**:70–80 (2016).

11. Sahai R, Miskimins J and Olson K, Laboratory results of proppant transport in complex fracture systems. *SPE Hydraulic Fracturing Technology Conference (SPE-168579)*. The Woodlands, Texas, USA, February 4–6 (2014).

12. Alotaibi M and Miskimins J, Slickwater proppant transport in complex fractures: new experimental findings & scalable correlation. *SPE Annual Technical Conference and Exhibition (SPE-174828)*, Houston, Texas, USA, September 28–30 (2015).

13. Tong S and Mohanty K, Proppant transport study in fractures with intersections. *Fuel* **181**:463–477 (2016).

14. Wang J, Sun B, Wang Z and Zhang J, Study on filtration patterns of supercritical CO_2 fracturing in unconventional natural gas reservoirs. *Greenhouse Gases Sci Technol* **7**(6):1126–1140 (2017).

15. Hou L, Sun B, Wang Z and Li Q, Experimental study of particle settling in supercritical carbon dioxide. *J Supercrit Fluids* **100**:121–128 (2015).

16. Guo B, Numerical simulation of the proppant transport in supercritical carbon dioxide fracturing. Master's thesis, China University of Petroleum, Beijing (2015).

17. Hou L, Sun B, Jiang X, Geng X, Wang Z and Li Q, Calculation on the following performance of proppant in supercritical CO_2. *Acta Petrol Sin* **37**:1061–1068 (2016). (In Chinese.)

18. Hou L, Jiang T, Liu H, Geng X, Sun B, Li G, *et al.*, An evaluation method of supercritical CO_2 thickening result for particle transporting. *J CO_2 Util* **21**:247–252 (2017).

19. ANSYS FLUENT 12.0 Theory guide, ANSYS Inc., pp. 558–569 (2009).

20. Han J, Yuan P, Huang X, Zhang H, Sookprasong A and Li C, Numerical study of proppant transport in complex fracture geometry. *SPE Low Perm Symposium (SPE-180243)*. Denver, Colorado, USA, May 5–6 (2016).

21. Kong X and McAndrew J, A computational fluid dynamics study of proppant placement in hydraulic fracture networks. *SPE Unconventional Resources Conference (SPE-185083)*. Calgary, Alberta, Canada, February 15–16 (2017).

22. Lun C, Savage S, Jeffrey D and Chepurniy N, Kinetic theories for granular flow: inelastic particles in Couette flow and slightly inelastic particles in a general flow field. *J Fluid Mech* **140**:223–256 (1984).

23. Johnson P and Jackson R, Frictional–collisional constitutive relations for granular materials with application to plane shearing. *J. Fluid Mech* **176**:67–93 (1987).

24. Heidaryan E and Jarrahian A, Modified Redlich Kwong equation of state for supercritical carbon dioxide. *J Supercrit Fluids* **81**(5):92–98 (2013).

25. Aungier R, A fast accurate real gas equation of state for fluid dynamic analysis applications. *J Fluids Eng* **117**(2): 277–281 (1995).

26. Kizaki A, Tanaka H, Ohashi K, Sakaguchi K and Matsuki K, Hydraulic fracturing in Inada granite and Ogino tuff with super critical carbon dioxide. *ISRM Regional Symposium – Seventh Asian Rock Mechanics Symposium*, Seoul, Korea, October 15–19 (2012).

27. Zhang T, Guo J and Liu W, CFD simulation of proppant transportation and settling in water fracture treatments. *Journal of Southwest Petroleum University (Science and Technology Edition)* **36**(1):74–82 (2014). (In Chinese.)

28. Liu Y, Settling and hydrodynamic retardation of proppants in hydraulic fractures. Doctoral dissertation, University of Texas at Austin, Austin (2006).

29. Wen Q, Gao J, Shao J, Wu P and Cheng X, Study on settlement law of proppant within horizontal wellbore in slick water fracturing, *Journal of Xi'an Shiyou University (Natural Science Edition)* **30**(4):73–78 (2015). (In Chinese.)

30. Wen Q, Duan X, Zhang Y, Liu H, Li Y and Wang S, Study on settlement and migration law of proppant in complex fracture network. *Journal of Xi'an Shiyou University (Natural Science Edition)* **31**(1):79–84 (2016). (In Chinese.)

Original Research Article: Numerical study of supercritical CO_2 and proppant transport in different geometrical fractures　　　H Wang *et al.*

13

31. Wen Q, Gao J, Liu H, Wang S and Wang F, Dynamic experiment on slick-water prop-carrying capacity. *Oil Drilling and Production Technology* **37**(2):97–100 (2015). (In Chinese.)

32. Li L, Experimental study of proppant transport and settling in fracturing fracture. Master's thesis, Southwest Petroleum University, Chengdu (2014).

Haizhu Wang

Haizhu Wang is an associate professor at the China University of Petroleum (Beijing), China, focusing on the application of supercritical CO_2 in unconventional gas reservoir drilling and fracturing, fluid mechanics in petroleum engineering, high pressure water jet, and so on. He has MSc and PhD degrees in oil and gas-well engineering from China University of Petroleum (Beijing).

Meng Wang

Meng Wang is a master's degree candidate at the China University of Petroleum (Beijing), focusing on proppant transport with supercritical CO_2 in fractures. He has a BSc from Northeast Petroleum University.

Bing Yang

Bing Yang is a master's degree candidate at the China University of Petroleum (Beijing), China, mainly focusing on the application of supercritical CO_2 fracturing in unconventional oil and gas reservoir development. He has a BSc degree from Xi'an Shiyou University, China.

Qun Lu

Qun Lu is a master's degree candidate at the China University of Petroleum (Beijing), China. His work focuses on the rules of proppant settlement and transport within horizontal wellbore in supercritical CO_2 fracturing. He has a BSc degree from China University of Petroleum (East).

Yong Zheng

Yong Zheng is a master's degree candidate at the China University of Petroleum (Beijing), focusing on the application of supercritical CO_2 in unconventional gas reservoir fracturing. He has a BSc from Northeast Petroleum University.

Heqian Zhao

Heqian Zhao is a PhD candidate at the China University of Petroleum (Beijing), China, focusing on fluid mechanics in petroleum engineering, solid-liquid two-phase flow in petroleum engineering, and so on. He has a bachelor's degree from the North East Petroleum University.